JGR Oceans

RESEARCH ARTICLE
10.1029/2025JC023420

Key Points:

- The coupled conditional nonlinear optimal perturbation method is utilized to identify sensitive areas of targeted observations
- The prediction uncertainties are more sensitive to initial errors in the wind field than to those in sea temperature
- The most sensitive area is located in the subsurface temperature in eastern Indian Ocean and wind field over the western Pacific

Correspondence to:
W. Duan,
duanws@lasg.iap.ac.cn

Citation:
Feng, R., Duan, W., & Hu, J. (2026). Identifying sensitive areas for targeted observations to improve Indian Ocean Dipole predictions using a coupled CNOP approach. *Journal of Geophysical Research: Oceans*, *131*, e2025JC023420. https://doi.org/10.1029/2025JC023420

Received 7 SEP 2025
Accepted 23 DEC 2025

Author Contributions:
Conceptualization: Rong Feng, Wansuo Duan
Data curation: Rong Feng
Formal analysis: Rong Feng, Wansuo Duan, Junya Hu
Funding acquisition: Rong Feng, Wansuo Duan
Investigation: Rong Feng, Junya Hu
Methodology: Wansuo Duan
Software: Rong Feng
Supervision: Wansuo Duan
Validation: Rong Feng, Junya Hu
Writing – original draft: Rong Feng
Writing – review & editing: Rong Feng, Wansuo Duan

Identifying Sensitive Areas for Targeted Observations to Improve Indian Ocean Dipole Predictions Using a Coupled CNOP Approach

Rong Feng[1], Wansuo Duan[1,2], and Junya Hu[3]

[1]State Key Laboratory of Earth System Numerical Modeling and Application, Institute of Atmospheric Physics, Chinese Academy of Sciences, Beijing, China, [2]Collaborative Innovation Center on Forecast and Evaluation of Meteorological Disasters (CIC-FEMD), Nanjing University of Information Science and Technology, Nanjing, China, [3]Key Laboratory of Ocean Circulation and Waves, Institute of Oceanology, Chinese Academy of Sciences, Qingdao, China

Abstract This study employs the coupled conditional nonlinear optimal perturbation (C-CNOP) method, which incorporates initial coupling uncertainties, to identify sensitive areas of targeted observations for positive Indian Ocean Dipole (IOD) events. Results show that the initial errors most likely to yield large prediction uncertainties of IOD events are mainly concentrated in sea temperatures near the thermocline in the eastern Indian Ocean (IO_Temp: 70–110 m depth, 5°S–5°N, 85°E−105°E) and western Pacific (PO_Temp: 120–160 m depth, 5°S–5°N, 130°E−150°E), as well as zonal winds (UWind), exhibiting an east–west dipole pattern over the tropical Indo-western Pacific. Through sensitivity experiments—designed to assess the impact of initial uncertainties in different areas on IOD predictions while bypassing the assimilation process and avoiding initial shock effects—we find that prediction uncertainties are more sensitive to initial errors in the UWind area than in the IO_Temp and PO_Temp areas, demonstrating a stronger impact on forecast skill, particularly in winter and summer. Further analysis demonstrated that the IO_Temp & PO_UWind coupled area involving the eastern Indian Ocean subsurface temperature and western Pacific zonal winds, exhibits greater sensitivity than the UWind area alone, emerging as the most sensitive area of positive IOD events. This key area highlights both the Pacific's remote influence and the crucial role of local ocean on IOD development. These results underscore the critical role of coupled initialization in IOD predictability, offering a theoretical basis for advancing coupled data assimilation.

Plain Language Summary The Indian Ocean Dipole (IOD) is an interannual air-sea coupled phenomenon in the tropical Indian Ocean that significantly influences global weather and climate. Accurate prediction of the IOD is therefore of great importance. However, the current skill of IOD forecasting is limited, partly due to inaccuracies in initial conditions. Given the constraints on observational resources, a critical challenge is to determine in which limited areas intensive observations should be conducted to enhance the accuracy of initial fields, thereby significantly improving IOD forecast skill. In this study, we employ the coupled conditional nonlinear optimal perturbation approach, which incorporates initial coupling uncertainties, to identify these sensitive areas. Our findings demonstrate that initial zonal wind errors over the tropical Indo-western Pacific have a more pronounced effect on prediction uncertainties than initial temperature errors in the IO_Temp (70–110 m depth, 5°S–5°N, 85°E−105°E) and PO_Temp (120–160 m depth, 5°S–5°N, 130°E−150°E) areas. Furthermore, we identify the coupled area—comprising eastern Indian Ocean subsurface temperature and western Pacific zonal winds—as the most sensitive area, which reflects both the remote influence from the Pacific and the crucial role of local ocean processes in IOD development. This study provides a theoretical foundation for the design of observation strategies in the Indo-Pacific region.

1. Introduction

The Indian Ocean Dipole (IOD) is a significant interannual air-sea coupling phenomenon over the tropical Indian Ocean, characterized by an east–west seesaw pattern of sea surface temperature anomalies (SSTAs) accompanied by anomalous wind fields in the equatorial region (Saji et al., 1999; Webster et al., 1999). During positive IOD events, severe droughts often occur in the eastern Indian Ocean, Indonesia, and Australia, while excessive rainfall is observed in the western Indian Ocean and East Africa; the impacts of negative IOD events are nearly the opposite (Li et al., 2021). Additionally, IOD events influence weather and climate in other regions globally through mechanisms such as the propagation of planetary waves (Qiu et al., 2014; Xiao et al., 2020; Yang

et al., 2010). With global warming, the tropical Indian Ocean has experienced a significant increase in the frequency of anomalous events, particularly those associated with the IOD, with a pronounced rise in the occurrence of strong IOD events (Cai et al., 2020; Hui & Zheng, 2018). Therefore, accurately predicting IOD events is crucial for improving weather and climate forecasting capabilities and formulating disaster prevention and mitigation measures. However, most current numerical models only provide skillful forecasts for IOD events one season in advance, with some extending to two seasons for strong IOD events (Luo et al., 2007; Shi et al., 2012; Zhu et al., 2015). Thus, achieving accurate forecasts for IOD events remains a significant challenge.

The low forecast skill of IOD events can be attributed to a variety of factors. First, IOD events are influenced by numerous complex physical processes, such as the strong Indian/Asian monsoon, interactions between IOD and El Niño–Southern Oscillation (ENSO), and stochastic intraseasonal oscillations in the atmosphere and ocean (Chen et al., 2021; Du et al., 2020; Huang et al., 2021; Jiang et al., 2021; Lu et al., 2018; Sang et al., 2019; Yang et al., 2015; Yuan et al., 2017; Zhang et al., 2015; Zhao et al., 2020). Second, most current models fail to accurately depict the fundamental characteristics of the tropical Indian Ocean climate state and IOD events, with limited capabilities in simulating and forecasting IOD events, leading to model errors (Feng et al., 2014). Furthermore, although the Indian Ocean Observing System (IndOOS) has been established over the tropical Indian Ocean, providing valuable data for mechanistic analysis of IOD and supporting model improvements and forecasting, the observational data remain relatively sparse. When assimilated into models, these observations introduce errors into the initial analysis fields. Feng et al. (2017) highlighted that east–west dipole-type initial sea temperature errors in the tropical Indian Ocean are most likely to cause the winter predictability barrier (WPB) for IOD events. Similarly, Liu et al. (2018) identified that initial sea temperature errors associated with the El Niño structure over the tropical Pacific are most likely to lead to rapid development of IOD forecast errors during summer, resulting in the summer predictability barrier (SPB). The WPB and SPB are characterized by a significant and rapid decline in forecast skills for the IOD region during winter or summer, regardless of the start month. Both the WPB and SPB severely limit the forecast skills for IOD events. However, these studies primarily focused on initial uncertainties in single oceanic variables, failing to fully account for the crucial role of initial ocean-atmosphere coupling errors and their impact on IOD predictability.

Deploying more observations and effectively assimilating observational data into numerical models are critical measures for reducing initial condition errors. However, the economic costs associated with large-scale, high-density observational deployments are often prohibitive. Targeted observations, also known as adaptive observations, offer a cost-effective alternative by focusing on strategically selected regions where additional data collection can significantly improve forecast accuracy. This approach has the potential to reduce prediction errors more effectively than an equivalent number of non-targeted observations. In other words, a relatively small number of strategically placed targeted observations can achieve error reduction comparable to that of a much larger array of non-targeted observations. Over the past decades, targeted observation strategy has been successfully applied to enhance forecast skill of various weather and climate events, including tropical cyclones (Kim et al., 2004; Mu et al., 2009; Qin & Mu, 2012), the ENSO (Yu et al., 2012), Kuroshio large meander (Wang et al., 2013). Furthermore, targeted observation strategy has been widely adopted in international field experiments to improve predictions of extreme weather events, including heavy rainfall, severe storms, and tropical cyclones (Burpee et al., 1996; Wu et al., 2005).

The identification of sensitive areas is a key aspect of targeted observation strategy. Researchers have developed various approaches to identify sensitive areas, which can be systematically categorized into two primary groups. The first group focuses on adjoint-based methods, which involve computing the adjoints of the forward tangent propagator of numerical models (Kim et al., 2004). This category includes well-established techniques such as singular vectors (SVs; Leutbecher & Palmer, 1998) and conditional nonlinear optimal perturbation (CNOP; Mu & Duan, 2003). The second group comprises ensemble-based approaches, featuring methods like the ensemble Kalman filter (Hamill & Snyder, 2002), the ensemble transform technique (Bishop & Toth, 1999), and the ensemble transform Kalman filter (Bishop et al., 2001).

Feng et al. (2017) have explored the sensitive areas of positive IOD events to advance beyond the WPB through perfect model predictability experiments. Their findings identified the subsurface layer of the eastern tropical Indian Ocean (5°S–5°N, 85°E−105°E) as a critical region (i.e., sensitive area) for targeted observations, where prediction uncertainties in winter are most sensitive to initial sea temperature errors in that region. Although Feng et al. (2017) successfully identified sensitive areas in the tropical Indian Ocean with respect to the WPB, their

study was limited to identifying these regions at a single depth level of 95 m, leaving the vertical distribution of sensitive areas unexplored. Liu et al. (2018) further highlighted that initial sea temperature errors in the tropical Pacific are most likely to trigger the SPB for IOD events, but they did not identify specific sensitive areas in the Pacific for targeted observations. Additionally, previous studies have primarily focused on the impact of sea temperature uncertainties on IOD predictability, with limited attention given to the role of wind field uncertainties in IOD forecasting. In particular, the important influence of the initial ocean-atmosphere coupling uncertainties among different variables is ignored. Therefore, it is essential to comprehensively assess the sensitivity of prediction uncertainties to different initial conditions, particularly considering the importance of initial ocean-atmosphere coupling uncertainties among different variables, to ultimately identify optimal observation regions. These investigations will not only deepen our understanding of IOD dynamics but also provide a theoretical foundation and scientific guidance for field observation campaigns and operational IOD forecasting.

Unlike conventional approaches, this study adopts the coupled CNOP (C-CNOP) method (Duan et al., 2024), which incorporates the effect of initial coupling uncertainties, to identify sensitive areas for IOD events. First, we examine the sensitivity of IOD prediction uncertainties to initial conditions of multiple variables, statistically determining the initial errors that have the greatest impact on prediction uncertainties. Next, by analyzing the spatial patterns of these initial errors, we identify potential sensitive areas for targeted observation. Finally, we compare the ensemble-mean forecasting skills based on different potential sensitive areas, thereby determining the optimal areas for targeted observation. The remainder of this paper is organized as follows: Section 2 introduces the model and methodology; Section 3 identifies of potential sensitive areas for targeted observation of IOD; Section 4 evaluates the effectiveness of these areas in enhancing IOD ensemble forecasting skills, and identifies the optimal sensitive areas; Section 5 presents a discussion of the results; and Section 6 provides a summary of the study.

2. Model and Methodology

2.1. Model

The geophysical fluid dynamics laboratory climate model version 2p1 (GFDL CM2p1) is used in this study, which is a fully coupled model integrating four key components: ocean, atmosphere, sea ice, and land. The ocean component is based on the Modular Ocean Model version 4 (MOM4p1; Griffies, 2009), which replaced the earlier MOM4.0 used in the CM2.1 version. This component is a numerical representation of the ocean's hydrostatic primitive equations, with a horizontal resolution of 1° × 1° and a refined meridional resolution of 1/3° in the equatorial region. Vertically, the ocean is divided into 50 layers, with a 10-m resolution in the upper 225 m. The atmospheric component, the GFDL Atmospheric Model (AM2p12b; GFDL Global Atmospheric Model Development Team, 2004), features a horizontal resolution of 2° (latitude) × 2.5° (longitude) and 24 vertical layers. The MOM4p1 ocean module and the AM2p12b atmospheric module are coupled with the Land Dynamics model version 2.1 (LM2.1; Milly & Shmakin, 2002) and the Sea Ice Simulator (SIS; Delworth et al., 2006) via the GFDL Flexible Modeling System (FMS; http://www.gfdl.noaa.gov/fms). Fluxes between these components are exchanged every 2 hours. Additional details about the model can be found in the works of Delworth et al. (2006), Stouffer et al. (2006), and Wittenberg et al. (2006).

Using the external forcings (aerosols, land cover, ozone, solar radiation, and radiative gases, etc.) in 1990, we conducted a 150-year integration of the GFDL CM2p1 model. The initial conditions for the ocean, atmosphere, land, and sea ice were consistent with those established by Delworth et al. (2006). After a 50-year spin-up period, the last 100 years of data were analyzed to eliminate the effects of the initial adjustment processes. Based on the definition of positive IOD events, where the Dipole Mode Index (DMI)—defined as the difference in SSTAs between the western and eastern poles (Saji et al., 1999)—exceeds 0.5°C for three consecutive months, we randomly selected 10 positive IOD events from the 100-year model data set. Analysis reveals that most positive IOD events exhibit a phase reversal of DMI during the preceding winter, reach their peak intensity in September-October of the event year, and subsequently decay with another DMI phase reversal in the following winter. This evolution pattern is consistent with observational findings (Wajsowicz, 2004), demonstrating the model's capability to realistically simulate the seasonal phase-locking characteristics of positive IOD events. Furthermore, Feng et al. (2014), through a comparative analysis of 14 models from the Coupled Model Intercomparison Project Phase 5 (CMIP5), identified GFDL CM2p1 as one of the most proficient models in simulating the fundamental characteristics of the Indian Ocean and IOD events. Therefore, the GFDL CM2p1 coupled model demonstrates

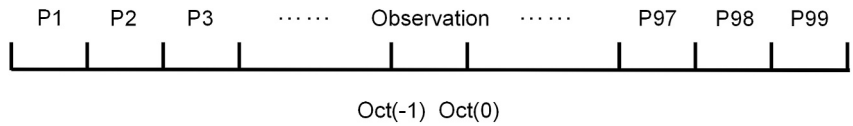

Figure 1. Schematic of the experimental design for one "observation" with start months October (−1). October (−1) along the *x*-axis indicates the first month of the observation. P1, P2, …, P99 indicate the 99 predictions for each "observation" with different initial conditions (where −1 denotes the year preceding the IOD event, and 0 denotes the year of the IOD event).

high skill in simulating both the climatology and interannual variability of the tropical Indian Ocean, providing a solid foundation for further investigation of IOD events, as detailed in the following sections.

2.2. Methodology

2.2.1. The C-CNOP Method

Climate variability is caused by complex interactions across the atmosphere, ocean, land, and other spheres. In numerical climate prediction, uncertainties stem from initial conditions in the ocean, atmosphere, sea ice, and land surface. In this study, we utilize the C-CNOP method proposed by Duan et al. (2024) to investigate the sensitivity of IOD prediction uncertainties to initial conditions of multiple variables and to identify the initial errors that exert the most significant statistical impact on IOD predictions. This approach systematically incorporates the combined effects of uncertainties from all initial conditions in the ocean, atmosphere, sea ice, and land surface, which more closely mirrors real-world forecasting scenarios. Through analysis of the spatial distribution characteristics of these initial errors, we preliminarily identify potential sensitive areas for targeted observations. Importantly, the C-CNOP method allows for the consideration of the effects of initial coupling uncertainties on IOD predictions, thereby offering an approach to identify coupling-sensitive areas. A concise overview of the method is provided below; for a more comprehensive understanding, readers are encouraged to consult Duan et al. (2024).

We randomly selected 10 positive IOD events from the 100-year integration to serve as the "observations." For each 1-year "observation," the remaining 99 years of data can be treated as 99 "predictions" with a lead time of 12 months. The predictions are initiated in October (−1), January (0), April (0), and July (0) (where −1 denotes the year preceding the IOD event, and 0 denotes the year of the IOD event). Among these, the predictions starting in October (−1) and January (0) bestride the winter and summer during the growing phase of IOD events, while those starting in April (0) and July (0) bestride the summer in the growing phase and the winter in the decaying phase. Taking October (−1) as an example, for a given positive IOD event, the data from October (−1) to September (0) represent the "observation," and the data from October (0) to September (+1) (where +1 denotes the year following the IOD event) are considered a "prediction" for that "observation." A total of 99 "predictions" are generated in this manner (Figure 1).

The prediction error is defined as the absolute difference in the DMI between the "prediction" and the corresponding "observation," denoted as A. The growth rates of prediction errors β are approximated as follows:

$$\beta = \frac{\partial A}{\partial t} \approx \frac{A_{t_2} - A_{t_1}}{t_2 - t_1} \tag{1}$$

where A_{t_2} and A_{t_1} are the prediction errors at times t_2 and t_1; the interval between t_1 and t_2 is 1 month. The seasonal mean of β represents the growth rate of the prediction errors for that season. A positive β signifies an increase in prediction errors for the season, while a negative β indicates a decrease; a larger positive β corresponds to a faster growth of prediction errors in that season. The calendar year is divided into four seasons: boreal winter (January–March), boreal spring (April–June), and so forth. For each "prediction," four β values are derived (one per season). Given that the external forcing fields remain constant, prediction errors arise solely from initial errors. Here, initial errors are defined as the differences between the initial fields of "predictions" and the corresponding "observation," which encompass components from the ocean, atmosphere, sea ice and land surface. Based on the definitions of WPB and SPB from the perspective of error growth dynamics (Feng et al., 2017; Liu et al., 2018), initial errors that yield the largest positive β during boreal winter or summer are selected as those most likely to induce a significant WPB or SPB. These initial errors represent the initial coupling uncertainties in the GFDL CM2p1 model that statistically exert the most significant impact on the prediction uncertainties of IOD events.

The substantial number of "predictions" ensures both diversity and statistical significance, indicating that these initial errors are identified based on a finite yet statistically robust set of "prediction" samples. According to the definition by Mu et al. (2003), CNOP is defined as the initial perturbation that satisfies specific physical constraints and leads to the largest prediction error at the forecast time. Duan et al. (2024) has demonstrated that the above limited number of but statistically significant prediction samples are used as constraints; therefore, these selected initial errors provides the statistically optimal coupled CNOP, referred to as C-CNOPs. For each starting month, a total of 10 C-CNOPs were derived, corresponding to 10 "observations." Additionally, initial errors leading to the 2nd to 5th highest growth rates in prediction errors during boreal winter or summer were also identified as fast-growing initial errors. This results in a total of 50 fast-growing initial errors for each starting month, which are also collectively termed C-CNOPs.

2.2.2. Forecast Skill Measures

In this study, we evaluate the deterministic forecast skill of IOD ensemble forecasting, where the ensemble members are generated based on different potential sensitive areas. Through this approach, we access the effectiveness of various potential sensitive areas in improving IOD forecast skills. Two key metrics of deterministic forecast skill are employed: the anomaly correlation coefficient (ACC), and root–mean–square error (RMSE). The ACC measures the forecast's ability to capture the evolution of the observed time series, while the RMSE quantifies the discrepancy between predictions and observations. These metrics are defined as follows:

$$\mathrm{ACC}(t)=\frac{\sum_{i=1}^{N}\left[x_i^o(t)-\overline{x^o}(t)\right]\left[x_i^p(t)-\overline{x^p}(t)\right]}{\sqrt{\sum_{i=1}^{N}\left[x_i^o(t)-\overline{x^o}(t)\right]^2}\sqrt{\sum_{i=1}^{N}\left[x_i^p(t)-\overline{x^p}(t)\right]^2}} \tag{2}$$

$$\mathrm{RMSE}(t)=\sqrt{\frac{1}{N}\sum_{i=1}^{N}\left[x_i^p(t)-x_i^o(t)\right]^2} \tag{3}$$

where x represents the variable of interest, p denotes the ensemble mean prediction, and o corresponds to observations. i and t indicate the different initial time and lead time of the prediction, respectively. N denotes the total number of initial conditions. In Equations 2 and 3, the overbar indicates the mean of all initial conditions. The ACC and RMSE quantify the overall deterministic forecast skill of all initial conditions as a function of lead time.

3. Identifying the Potential Sensitive Areas of IOD Events

For each starting month, a total of 50 C-CNOPs were obtained, incorporating initial error components from the oceanic, atmospheric, sea ice, and land surface systems. Our analysis focused on initial errors in sea temperature and wind field components that are closely associated with the evolution of IOD events, and initial errors within these fields probably greatly impact the prediction uncertainties. We performed combined Empirical Orthogonal Function (C-EOF) analysis on both the upper 200-m sea temperature components and the 500–1,000 hPa wind field components derived from these C-CNOPs. The leading EOF mode (EOF1) represents the dominant spatial patterns of initial coupling uncertainties that are most likely to cause predictability barriers for IOD events at different starting months. As shown in Figure 2, the spatial distribution of these initial sea temperature errors exhibits a distinct east–west dipole pattern in the tropical Indian Ocean consistent with Feng et al. (2017). Simultaneously, a dipole pattern is observed in the tropical Pacific, characterized by subsurface anomalies in the western Pacific and upper-layer anomalies in the eastern Pacific, aligning with Liu et al. (2018). Their large values are primarily concentrated near the thermocline in the eastern Indian Ocean and the western Pacific. Similar conclusions were obtained across different starting months. This suggests that initial sea temperature errors in these regions may significantly contribute to prediction uncertainties of IOD events, indicating particular sensitivity of prediction errors to initial sea temperature errors in these areas. Consequently, these regions represent potential sensitive areas for targeted observation in IOD predictions.

Meanwhile, the dominant spatial modes of initial wind field errors are analyzed. Taking starting month October (−1) as an example, Figure 3 illustrates that initial errors in zonal wind components are significantly larger than those in meridional wind components, highlighting the critical role of initial zonal wind errors in IOD predictions.

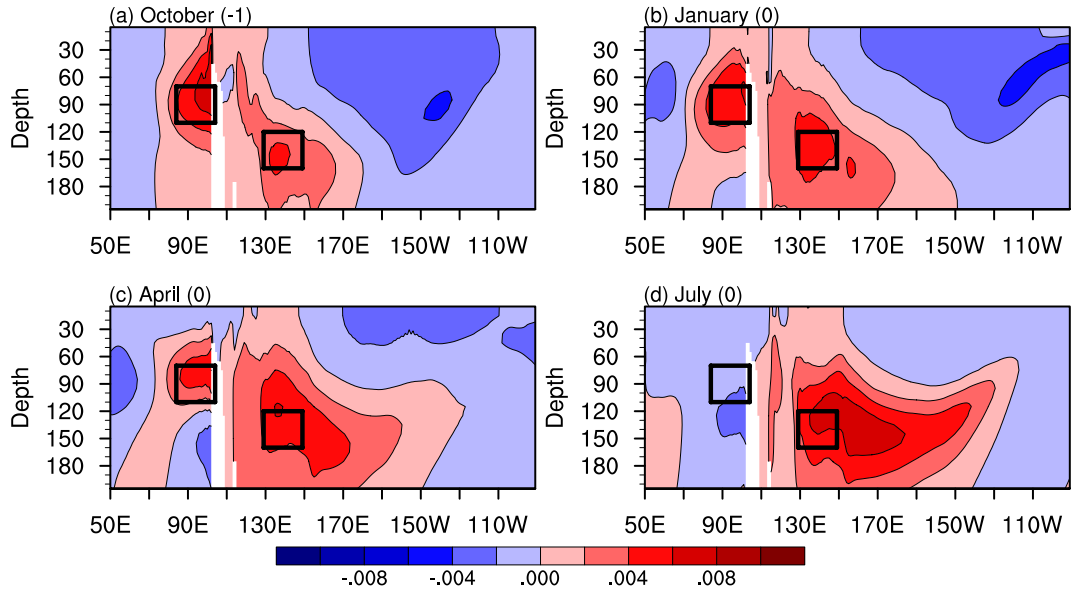

Figure 2. Equatorial (5°S–5°N) initial sea temperature errors for the leading mode of the C-EOF analysis of C-CNOPs, shown for the starting months of (a) October (−1), (b) January (0), (c) April (0), and (d) July (0). Black boxes represent the areas where the large values of the dominant pattern are located. (units: °C).

These errors exhibit a distinct east–west dipole pattern over the tropical Indian Ocean and Pacific Ocean, which are well coupled with the initial sea temperature errors in Figure 2. The initial errors exhibit localized characteristics, with large values mainly concentrated over the tropical Indian Ocean and tropical western Pacific regions, respectively. This spatial distribution suggests that initial zonal wind errors in these specific regions make substantial contributions to IOD prediction uncertainties, indicating particular sensitivity of prediction errors to initial zonal wind errors in these areas. Consequently, these areas may represent potential sensitive areas for targeted observation in IOD forecasting. While the dominant error patterns consistently maintain dipole modes over the Indian and Pacific Oceans for starting months January (0), and April (0), the large-value areas vary with different starting months. In addition to the dipole-pattern areas identified above, a large-value area is also present at 500 hPa; however, it is demonstrated to be insensitive and is therefore excluded from further discussion (figure omitted). Furthermore, for starting month July (0), the large values are mainly concentrated over the Indo-Pacific warm pool. This suggests that the optimal locations for wind field observations may vary depending on the starting months of IOD predictions.

To ensure a fair comparison of the impacts of initial sea temperature and wind field uncertainties on IOD predictions, we defined three potential sensitive areas, each containing an equal number of grid points: the Indian Ocean temperature area (IO_Temp), the Pacific Ocean temperature area (PO_Temp), and the zonal wind area (UWind). The large-value areas of initial sea temperature errors in Figure 2 were defined as IO_Temp (70–110 m depth, 5°S–5°N, 85°E−105°E) and PO_Temp (120–160 m depth, 5°S–5°N, 130°E−150°E). The wind field sensitive areas vary with starting months. For the starting month of October (−1), two large-value areas were identified: IO_UWind (5°S–5°N, 55°E−95°E, 550–1,000 hPa) and PO_UWind (5°S–5°N, 140°E−155°W, 700–950 hPa). For the starting of month January (0), the large-value areas are primarily located at IO_UWind (5°S–5°N, 60°E−90°E, 500–1,000 hPa) and PO_UWind (5°S–5°N, 125°E−155°E, 500–1,000 hPa). For the starting month of April(0), the main large-value areas are IO_UWind (5°S–5°N, 90°E−130°E, 500–900 hPa) and PO_UWind (5°S–5°N, 140°E−175°E, 600–1,000 hPa). For the starting month of July (0), the large-value areas are primarily concentrated in IO_UWind (5°S–5°N, 115°E−147°E, 450–985 hPa) and PO_UWind (5°S–5°N, 148°E−180, 450–985 hPa). IO_UWind and PO_UWind are collectively referred to as UWind.

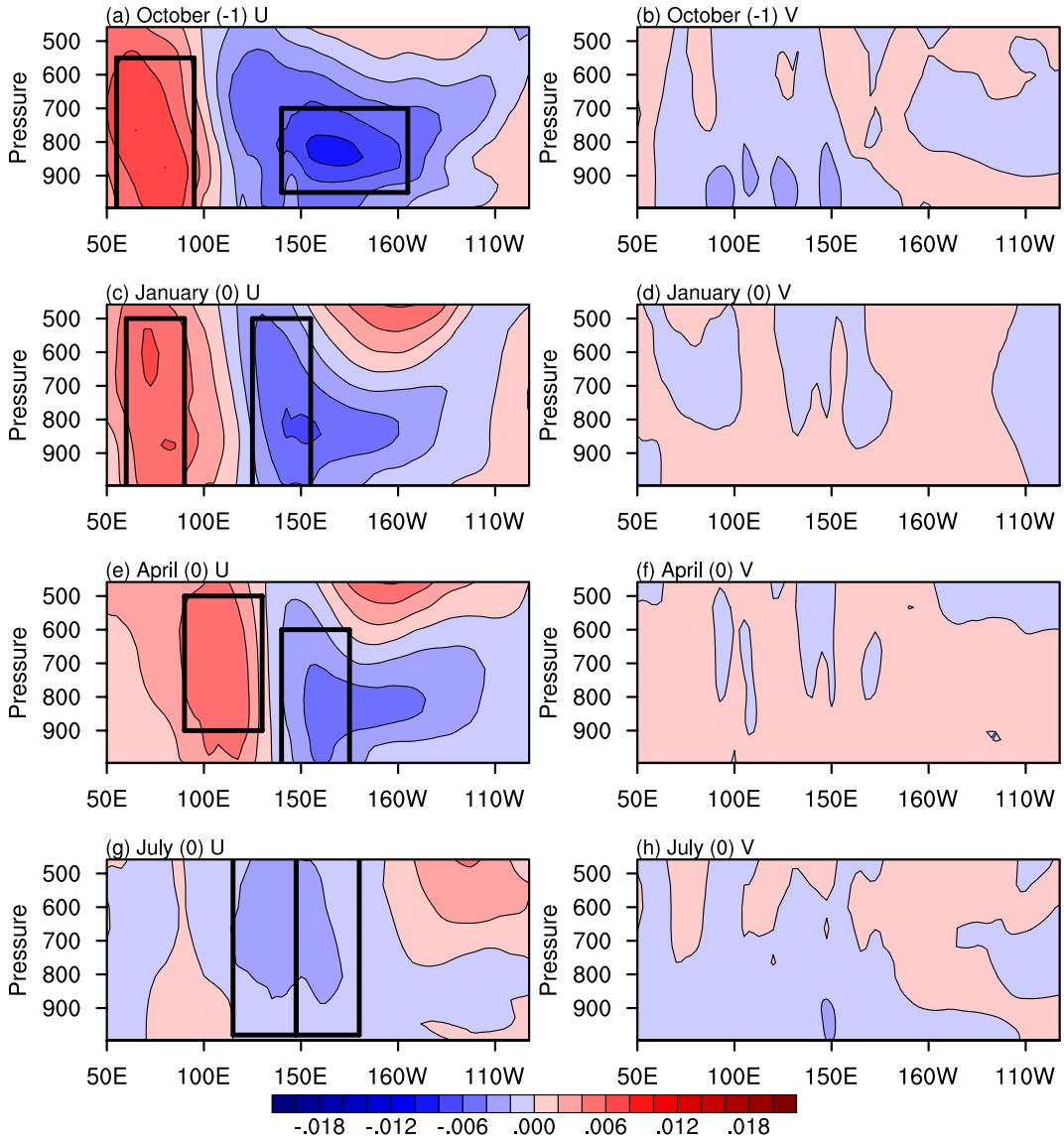

Figure 3. Initial zonal wind errors (left panels) and meridional wind errors (right panels) along the equator (5°S–5°N) for the leading mode of the C-EOF analysis of C-CNOPs. Results are shown for the starting months of (a, b) October (−1), (c, d) January (0), (e, f) April (0), and (g, h) July (0). Black boxes represent the areas where the large values of the dominant pattern are located. (units: m/s).

4. Evaluating the Effectiveness of Potential Sensitive Areas in Enhancing IOD Forecast Skill

In Section 3, we identified several potential temperature and wind field sensitivity areas. However, two key questions remain unresolved: (a) Are these areas truly the sensitive areas of IOD events? In other words, can enhancing the initial field accuracy within these areas effectively improve IOD forecast skill? (b) Among them, which area is the most sensitive? To address these questions, we conducted a series of idealized experiments.

We selected 10 positive IOD events from the 100-year GFDL CM2p1 model simulation to serve as "observations" (identical to those analyzed in Section 2). For each 1-year "observation," the remaining 99 years of model data were treated as 99 "predictions" with a 12-month lead time, initialized in October (−1), January (0), April (0), and July (0). Since these "predictions" differ solely due to variations in initial conditions, they effectively represent ensemble forecast members integrated from different initial fields. The full collection of 99 "predictions" serves as the "original" ensemble forecast.

According to the definition of targeted observations, enhancing initial field accuracy by assimilating additional observations within sensitive areas—rather than observations in other regions with the same number of grid points—should more effectively improve forecast skill. Furthermore, if an initial field exhibits sufficient similarity to the "observation" within a given area, it can be interpreted that this initial field was derived through the assimilation of observational data in that area. Consequently, initial fields that exhibit similarity to "observations" within sensitive areas will yield superior forecast skill compared to those showing similarity in other regions, particularly in the absence of model errors, as assumed in this study. For each "observation," we selected "predictions" whose initial fields showed strong similarity to the "observation" within different potential sensitive areas, based on two selection criteria: (a) spatial correlation coefficients between the initial fields of "prediction" and "observation" within the potential sensitive area exceeding 0.7, and (b) initial field errors within the potential sensitive area lower than the root mean square error across all "predictions." A sensitivity test employing stricter and more lenient criteria confirmed that main conclusions remain unchanged, indicating the robustness of our primary conclusions. These selected individual "predictions" formed "new" ensemble forecasts corresponding to different potential sensitive areas. We then quantified forecast skill using ensemble forecast metrics. Through comparative analysis of forecast skill across different potential sensitive areas—including assessment of improvements relative to the "original" ensemble forecast—we evaluated their relative effectiveness in improving the forecast skill of IOD events. Regions yielding the highest forecast skill were identified as the most sensitive. Unlike conventional Observing System Simulation Experiment (OSSE) or Observing System Experiment (OSE) experiments, our approach eliminates the influence of model errors, bypasses the assimilation process, and avoids initial shock effects. This allows for a more direct assessment of how initial uncertainties in different potential sensitive regions impact IOD predictions.

4.1. Evaluating the Relative Effectiveness of Potential Sea Temperature and Wind Field Sensitive Areas in Enhancing IOD Forecast Skill

Using a single "observation" as an example, we first examine the relationship between prediction errors and initial field similarity in different potential sensitive areas, providing a preliminary assessment of the sensitivity of prediction uncertainties to initial errors in these areas. For each starting month, we calculated correlation coefficients between initial fields of 99 "predictions" and "observation" within each potential sensitive area, along with their corresponding prediction errors. Figure 4 shows scatter plots of correlation coefficients versus prediction errors for different potential sensitive areas. The results reveal that for forecasts initialized in October (−1) and July (0), a strong inverse relationship exists for the IO_Temp area—specifically, higher correlation coefficients correspond to smaller prediction errors, and vice versa. This implies that when the initial sea temperature fields of "predictions" more closely resemble the "observation" within the IO_Temp area, the prediction errors are smaller. Consequently, improving the accuracy of initial sea temperature fields in the IO_Temp area- by assimilating additional observations there, could help reduce prediction errors and improve IOD forecast skill. Moreover, the corresponding trend lines exhibit the steepest slopes, suggesting that prediction uncertainties are most sensitive to initial errors in this area. In contrast, for the starting months January (0) and April (0), the UWind area exhibits a more consistent and robust correlation-error relationship with the largest absolute slopes of tend lines, where data points cluster tightly around the trend line. These results indicate that prediction uncertainties are most sensitive to initial errors in the UWind area for these starting months.

These different sensitivities fundamentally stems from the strongly season-dependent physical processes governing the development and decay of the IOD. For the starting month October (−1), an IOD event is only a potential outcome. The subsurface heat content in the eastern Indian Ocean (the IO_Temp area) acts as the primary "energy reservoir" for a possible future event. While atmospheric field sensitivity exists, the wind field is not yet organized, making oceanic thermal conditions more influential than winds at this stage. For the starting months January (0) and April (0), the Bjerknes positive feedback is becoming active. The wind field acts as the "engine" of the Bjerknes feedback. Erroneous westerly anomalies over the Indian Ocean would suppress upwelling, warm the eastern basin, and potentially abort a developing positive IOD event. Besides, wind errors over the western Pacific can alter the Walker circulation, inducing subsidence or uplift over the Indian Ocean, thereby enhancing or suppressing IOD growth. Therefore, errors in the wind field can rapidly disrupt the Bjerknes feedback, making winds more sensitive than the ocean's initial thermal state. For the starting month July (0), the event is already well-developed, and the ocean and atmosphere are tightly locked in a positive feedback. Errors in the eastern Indian Ocean subsurface (IO_Temp) become critical, as they directly affect the maintenance of the

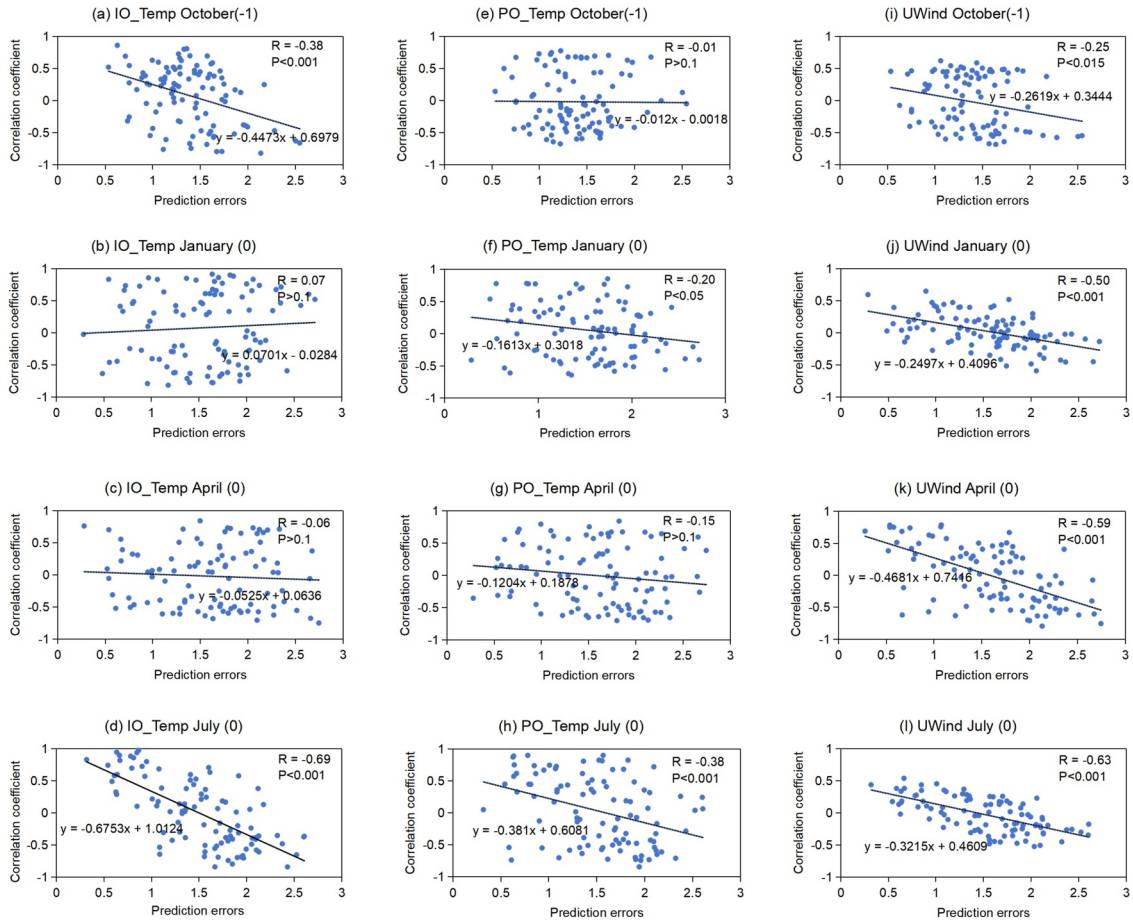

Figure 4. Scatter plots illustrating the relationship between correlation coefficients and prediction errors for the IO_Temp, PO_Temp, and UWind areas for different start months. The correlation coefficients were calculated between initial fields of 99 "predictions" and their corresponding "observation" within each potential sensitive area. The linear best fits (solid lines) are displayed together with the correlation coefficient R (correlation—error) and *P* value from the regression.

surface cold tongue via upwelling. At this stage, the system is so strongly coupled that errors in either the ocean or wind field can cause significant disruption, especially in the IO_Temp area, resulting in high sensitivity.

To further quantitatively evaluate the relative effectiveness of potential temperature and wind field sensitive areas in improving IOD forecast skill, we constructed "new" ensemble forecasts by selecting members from the 99 "predictions" that exhibited both high initial-field correlation and low errors in the three key areas. Taking one "observation" as an example, Figures 5a–5d display the DMI evolution for both selected ensemble members and their ensemble mean for the IO_Temp area. The results show that for the starting months October (−1) and April (0), although a few members predicted the positive IOD event, the "new" ensemble mean forecast showed no significant improvement over the "original" ensemble mean forecast, even exhibiting lower skill in some months. For other starting months, a number of members successfully captured the positive IOD event, with the "new" ensemble mean forecast outperforming the "original" ensemble mean forecast. The most dramatic enhancement occurred for the starting month July (0), where most selected members accurately predicted the observed positive IOD event, demonstrating substantially higher skill than the "original" ensemble mean forecast. These results indicate that to improve the accuracy of initial fields in the IO_Temp areas-particularly for the starting month July (0)- can largely improve the IOD forecast skill. This demonstrates that prediction uncertainties of IOD events are sensitive to initial errors in the IO_Temp area, especially for the starting month July (0). However, the finding that some members with excellent initial-field correlations (>0.9) still failed to predict the event in other starting months suggests that while the IO_Temp area is important, it may not represent the most critical sensitive area for IOD prediction. In contrast, the PO_Temp area exhibited higher forecast skill for the starting month April (0), but lower skill for July (0) (Figures 5e–5h). Notably, most ensemble members for the UWind area consistently and

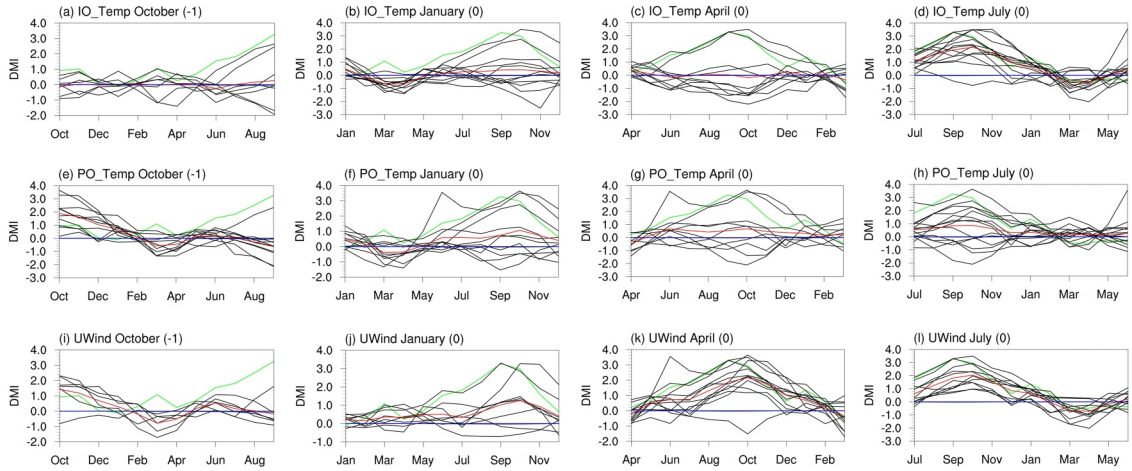

Figure 5. Evolution of the DMI in selected ensemble members (black lines), their mean (red lines), observations (green lines), and the "original" ensemble mean (blue lines) for three sensitivity areas (IO_Temp, PO_Temp, and UWind). The starting months are October(−1), January(0), April(0), and July(0), where −1 indicates the year preceding the IOD event and 0 denotes the event year, respectively.

accurately predicted positive IOD events across all starting months, significantly outperforming those for both the IO_Temp and PO_Temp areas. This indicates that IOD prediction uncertainties are highly sensitive to initial errors in the UWind area. Consequently, precise initialization of initial wind field in this area can probably lead to successful IOD predictions, even at long lead times. This finding complement and significantly extend previous studies by revealing a previously underappreciated dominance of wind field uncertainties (Feng et al., 2017; Liu et al., 2018; Luo et al., 2007; Wajsowicz, 2005).

The improvement of "new" ensemble forecasts over the "original" ensemble forecasts was quantitatively assessed in Figure 6, which displays *IMPACT* values for different potential sensitive areas. *IMPACT* is defined as the difference in prediction errors between the "new" and "original" ensemble mean forecasts, where a negative value signifies reduced errors and improved forecast skill. As illustrated in the figure, *IMPACT* is predominantly negative across most starting months, indicating that the "new" ensemble forecast—derived from different potential sensitive areas—generally improves forecast skill. The sole exception is the starting month October (−1), where skill is not almost improved. This is because, the predictable signal in October (−1) is too weak relative to the inherent noise—such as random intraseasonal variability, unpredictable weather events. Although observations assimilated in these areas capture the initial state, forecast skill remains limited. Moreover, these predictions span both the SPB and the WPB. Over such a long duration, even small initial uncertainties can amplify through these barriers, resulting in large prediction uncertainties. A comparative analysis further reveals that for the starting months January (0) and April (0), the UWind area exhibits the largest absolute *IMPACT* values and yields the highest forecast skill. Conversely, for October (−1) and July (0), the IO_Temp area demonstrates higher forecast skill, and the UWind area exhibits values comparable to those of the IO_Temp area. This pronounced improvement underscores the UWind area's critical role in IOD prediction, suggesting that prioritizing accurate initialization in this region could substantially enhance forecast skill. Furthermore, since the UWind area composes both the IO_UWind and PO_UWind areas, we further compare their relative contributions (figure omitted). The *IMPACT* values show that the PO_UWind area presents absolute values slightly lower than those of the UWind area but still significantly higher than those of the IO_UWind area. This indicates that zonal wind over the western Pacific Ocean plays a more important role in IOD prediction than that over the Indian Ocean, especially at longer lead times.

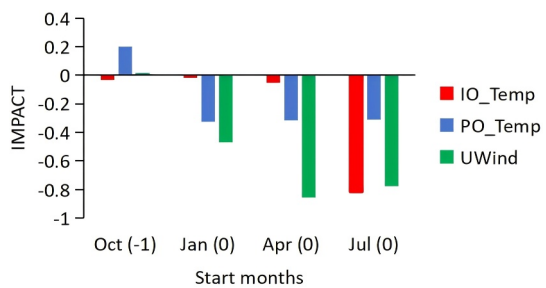

Figure 6. Annual mean *IMPACT* values for three sensitivity areas (IO_Temp, PO_Temp, and UWind). *IMPACT* quantifies the difference in prediction errors between the "new" and "original" ensemble mean forecasts. Results are shown for initialization in October(−1), January(0), April(0), and July (0), where −1 indicates the year preceding the IOD event and 0 denotes the event year, respectively.

Then, how do these "new" ensemble forecasts influence forecast skill in winter and summer and, consequently, the WPB and SPB phenomena? To further address this question, we calculated *IMPACT-S*, which measures the

Figure 7. *IMPACT-S* values in winter (JFM) and summer (JAS) for three areas (IO_Temp, PO_Temp, and UWind). *IMPACT-S* signifies the prediction error differences between the "new" and "original" ensemble mean forecasts. Results are organized by starting months: October(−1), January(0), April(0), and July(0), where −1 indicates the year preceding the IOD event and 0 denotes the event year, respectively.

difference in prediction errors between the "new" and "original" ensemble mean forecasts for winter and summer across different potential sensitive areas (Figure 7). Negative values signify reduced errors and improved forecast skill. The "new" ensemble mean forecasts for the UWind area significantly reduce winter prediction errors across the most starting months, thereby mitigating the WPB phenomenon and improving forecast skill. In comparison, the ensemble mean forecasts for the IO_Temp area also reduce winter prediction errors, though to a lesser extent, while, the forecasts for the PO_Temp area show the smallest improvement. This suggests that winter prediction uncertainties are most sensitive to initial errors in the UWind area, followed by the IO_Temp area. Summer prediction uncertainties show similar primary sensitivity to initial errors in the UWind area, but secondary sensitivities to those in the IO_Temp and PO_Temp areas. These results regarding the sea temperature initialization impacts are consistent with previous studies (Feng & Duan, 2019; Feng et al., 2017; Liu et al., 2021). However, they ignored the primary role of wind initialization. Our findings imply that assimilating additional observations in the UWind area (followed by the IO_Temp area) to enhance initial field accuracy would largely reduce winter and summer prediction errors and mitigate the WPB and SPB phenomena.

The preceding discussion focused on a single "observation" case. To strengthen our findings, we now expand the analysis to include 10 "observations." The results confirm that the core conclusions remain consistent with the earlier analysis. Furthermore, we evaluate the deterministic forecast skill of "new" ensemble forecasts, and access the effectiveness of various potential sensitive areas in improving IOD forecast skills. We analyze their ACC and RMSE across different potential sensitive areas, as illustrated in Figure 8. Using ACC > 0.5 as the threshold for skillful forecasts, the IO_Temp area performs well at shorter lead times, successfully predicting IOD events up to 4 months in advance. This is primarily because, the initial oceanic memory in the Indian Ocean plays a significant role at shorter lead times. As the lead time increases, the influence of initial local oceanic memory gradually diminishes. Crucially, IOD evolution is not merely a local process; it is also modulated by remote wind forcing from the tropical Pacific. When models fail to accurately capture this critical remote influence from the Pacific, such deficiencies rapidly amplify, leading to substantial prediction errors and low forecast skill. As a result, forecast skill declines significantly at longer lead times. The PO_Temp area, though initially less skillful than the IO_Temp area, maintains relatively high ACC values over longer lead times. Notably, the UWind area outperforms the others, and the lead time of skillful forecast extends to 10 months—significantly longer than other areas. Consistent with the ACC results, the UWind area also exhibits the smallest RMSE, further confirming its superior forecast skill. In contrast, the IO_Temp and PO_Temp areas show higher RMSE values, aligning with their respective ACC performance trends. These findings robustly demonstrate that the UWind area yields the highest forecast skill for IOD predictions. Consequently, we conclude that this area is the sensitive area for IOD predictions. Enhancing the accuracy of initial conditions in this area would most effectively enhance IOD forecast skill.

4.2. Evaluating the Effectiveness of Coupled Sensitive Areas in Enhancing IOD Forecast Skill

Building on our previous analysis comparing the relative impacts of initial sea temperature and wind field uncertainties on IOD predictions, we established that the UWind area is the most sensitive for IOD predictions. However, in operational forecasting, initial uncertainties typically occur across multiple coupled spheres rather

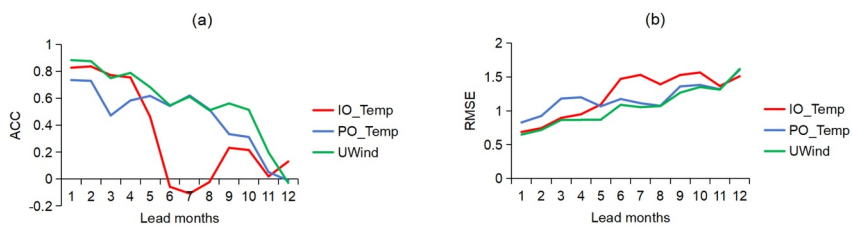

Figure 8. (a) ACC and (b) RMSE of the DMI compared with the observations. The results are for three sensitivity areas: IO_Temp (red lines), PO_Temp (blue lines), and UWind (green lines).

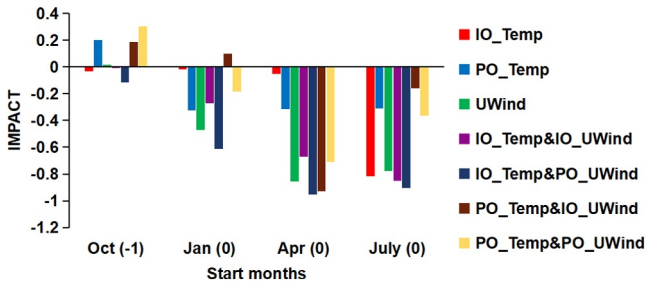

Figure 9. Annual mean *IMPACT* values for different potential sensitivity areas. *IMPACT* quantifies the difference in prediction errors between the "new" and "original" ensemble mean forecasts. Results are shown for initialization in October(−1), January(0), April(0), and July(0), where −1 indicates the year preceding the IOD event and 0 denotes the event year, respectively.

than being isolated to the wind field alone. To understand how initial coupling uncertainties affect IOD predictability, we examine four dynamically coupled areas for each starting month: IO_Temp&IO_UWind, IO_Temp&PO_UWind, PO_Temp&IO_UWind, and PO_Temp&PO_UWind. These combinations integrate the previously identified sea temperature and wind field sensitivity areas for each respective starting month.

Using a representative observational case, we constructed "new" ensemble forecasts by selecting members from the 99 "predictions" that exhibited both high initial-field correlation and low errors in the four coupled areas. Figure 9 quantitatively evaluates the improvement of these "new" ensemble forecasts over the "original" ensemble through *IMPACT* analysis for different starting months. *IMPACT* is negative across most starting months, indicating that the "new" ensemble forecasts—derived from different potential sensitive areas—generally improve forecast skill. The primary exception is the starting month October (−1), where *IMPACT* values are positive for some areas, indicating a reduction in forecast skill. However, the IO_Temp&PO_UWind area presents a notably negative *IMPACT* value for this starting month, indicating a clear improvement in forecast skill. Further comparative analysis reveals that, the IO_Temp&PO_UWind area yields the largest absolute *IMPACT* values across all starting months, indicating the highest forecast skill-significantly outperforming the UWind area. These findings underscore that incorporating initial coupling uncertainties improves forecast skill, particularly in the "new" ensemble forecast derived from the IO_Temp&PO_UWind area, emphasizing the critical importance of properly accounting for initial coupling uncertainties.

Furthermore, we assess the deterministic forecast skill of "new" ensemble forecasts across all the 10 "observations." By analyzing their ACC and RMSE for each potential sensitive area (Figure 10), we find that the IO_Temp&PO_UWind region consistently outperforms others at all lead times. Using ACC > 0.5 as the threshold for skillful forecasts, the IO_Temp&PO_UWind area successfully predicts IOD events up to 10 months in advance, exhibiting systematically higher ACC values than the previously validated UWind sensitive area (as established in Section 4.1). Moreover, it exhibits the lowest RMSE among all potential sensitive areas, further validating its superior forecast skill. These results strongly indicate that the IO_Temp&PO_UWind area yields the highest forecast skill for IOD predictions. We therefore conclude that this area represents the most sensitive area for IOD predictions. Improving the accuracy of initial conditions in this area, through targeted observations and their assimilation into numerical models would most effectively improve IOD forecast skill.

By comparing forecast results based on the IO_Temp&PO_UWind sensitive area (illustrated using one forecast member) with those from other coupled areas (e.g., PO_Temp&IO_UWind) against one "observation," we analyze why the IO_Temp&PO_UWind area exhibits higher sensitivity. In other words, why does improving initial field accuracy in this area lead to higher IOD forecast skill? Figure 11 presents the evolution of SST and lower-level wind field anomalies initialized in January. In the initial fields (January), the forecast member for the IO_Temp&PO_UWind area shows strong consistency with "observation" over the western Pacific, where exhibits anomalous southwesterly winds. However, over the Indian Ocean, this member displays northeasterly wind anomalies, different from the "observation." In contrast, the PO_Temp&IO_UWind member closely matches the

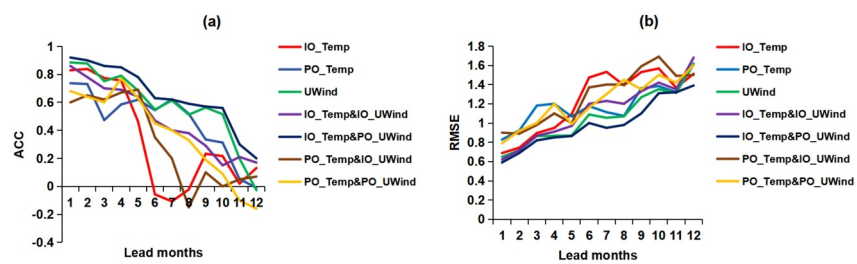

Figure 10. (a) ACC and (b) RMSE of the DMI compared with the observations. The results are for different potential sensitivity areas: IO_Temp (red lines), PO_Temp (blue lines), UWind (green lines), IO_Temp&IO_UWind (purple lines), IO_Temp&PO_UWind (dark blue lines), PO_Temp&IO_UWind (brown lines), and PO_Temp&PO_UWind (yellow lines).

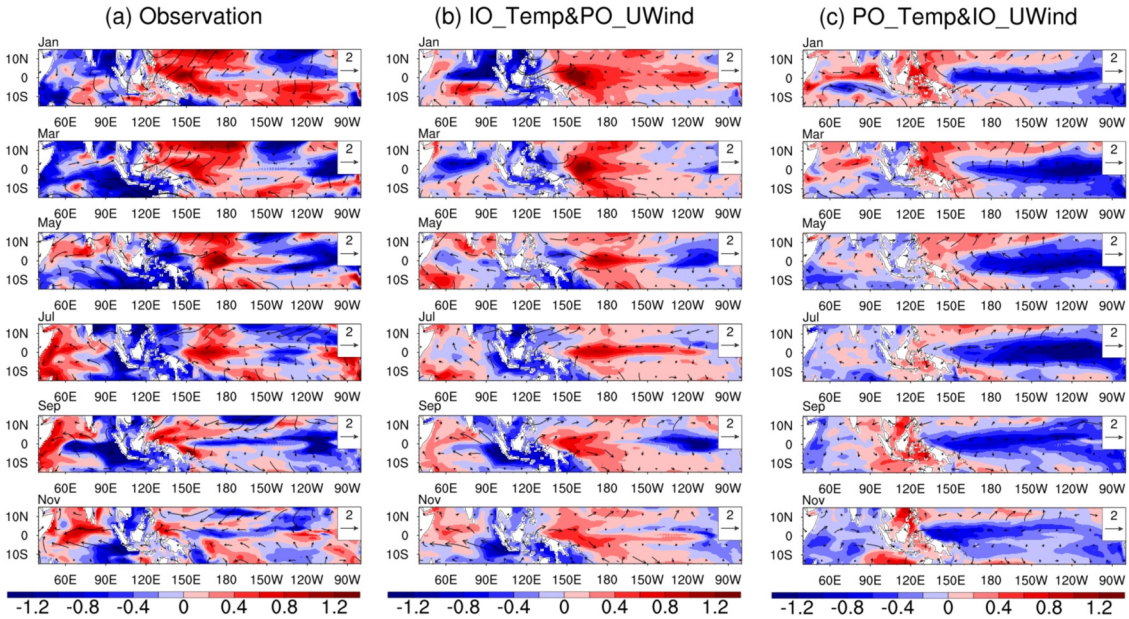

Figure 11. Evolution of SST (°C, shading) and lower-level wind field anomalies (m/s, vectors) initialized from January, comparing forecast members based on (b) the IO_Temp&PO_UWind sensitive area, (c) the PO_Temp&IO_UWind area, and (a) the "observation."

observed northwesterly wind anomalies over the Indian Ocean but diverges in the western Pacific, producing anomalous southeasterly and northeasterly winds instead. This raises the first question: Which factor is more critical for accurately predicting a positive IOD event—correctly capturing the western Pacific wind field (i.e., IO_Temp&PO_UWind area) or the Indian Ocean wind field (i.e., PO_Temp&IO_UWind area)? Furthermore, a comparable analysis was conducted for subsurface temperature anomaly distributions (figure omitted). The IO_Temp&PO_UWind member successfully captures the observed negative temperature anomalies in the eastern Indian Ocean, whereas the PO_Temp&IO_UWind member captures the subsurface temperature anomalies in the western Pacific but fails to reproduce the cold anomalies in the eastern Indian Ocean. Consequently, another key question emerges: Which factor is more important for IOD prediction—correctly capturing the subsurface temperature anomalies in the eastern Indian Ocean or western Pacific? Our comparative analysis demonstrates that the forecast member for the IO_Temp&PO_UWind area correctly captures the observed anomalous wind field over the western Pacific at the initial time, which subsequently perturbs the Walker circulation, and induces anomalous subsidence over the eastern Indian Ocean (Figure 12b), which is consistent with "observation." This subsidence leads to surface wind divergence, promoting upwelling of cold subsurface water. Concurrently, the observed negative subsurface temperature anomalies in the eastern Indian Ocean further amplify this cooling through enhanced upwelling, favoring the development of a positive IOD event. Conversely, the forecast member for the PO_Temp&IO_UWind area generates anomalous southeasterly/northeasterly winds over the western Pacific. These winds induce anomalous ascent over the eastern Indian Ocean (Figure 12c). In combination with the positive subsurface temperature anomalies in the eastern Indian Ocean, this setup favors warming in the eastern Indian Ocean, ultimately leading to a negative IOD event. This set of comparative cases indicates that, the IO_Temp&PO_UWind member can successfully predict the observed positive IOD despite large initial wind field errors over the Indian Ocean. In contrast, the PO_Temp&IO_UWind member, despite accurately captures Indian Ocean wind field, fails to predict the positive IOD due to incorrect wind field over the western Pacific. These results highlight the greater importance of initial wind fields over the western Pacific. Similarly, it is found that accurately simulating subsurface temperature in the eastern Indian Ocean is more critical for IOD forecasting than that in the western Pacific. This highlights the greater importance of eastern Indian Ocean subsurface temperature. The identified coupled sensitive area accounts for both the Pacific's remote influence on IOD development—consistent with prior studies (Yang et al., 2015; Zhang et al., 2015)—and the crucial role of local ocean. This underscores the necessity of considering initial coupling uncertainties to improve IOD forecast skill, reaffirming the value of coupled sensitive area analysis.

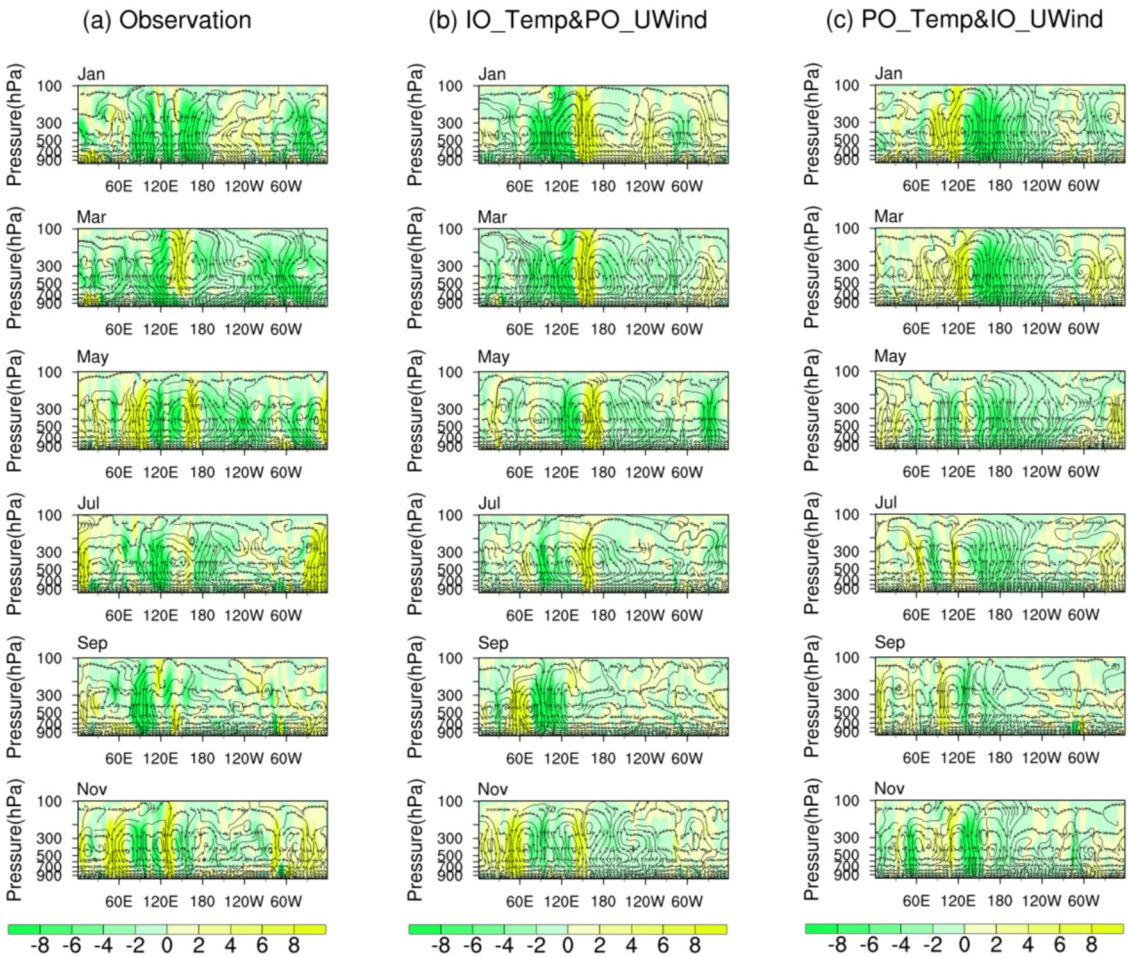

Figure 12. Evolution of the Walker circulation anomalies (arrow; the vertical velocity component has been multiplied by 400) and the vertical velocity anomalies (shaded; units: 1/400 Pa/s) initialized from January, comparing forecast members based on (b) the IO_Temp&PO_UWind sensitive area, (c) the PO_Temp&IO_UWind area, and (a) the "observation." The zonal average is taken over 10°S–10°N.

5. Discussion

Feng et al. (2017) investigated the impact of initial sea temperature uncertainties on IOD predictability, and identified a sensitive area for targeted observation, located mainly in the eastern tropical Indian Ocean (5°S–5°N, 85°E−105°E) at a depth of 95 m. They suggested that conducting intensive observations in this specific area, compared to other oceanic areas, could more effectively improve the forecast skill of IOD events. In the present study, we compare the relative importance of initial sea temperature and wind field uncertainties on IOD predictability. Our results demonstrate that initial wind field uncertainties, particularly in the zonal component over the western Pacific, exert a greater influence on IOD prediction than initial sea temperature uncertainties. Furthermore, we explore the effect of initial air-sea coupling uncertainties on IOD predictability and identify a coupled sensitive area, referred to as the IO_Temp&PO_UWind. It is noted that, this coupled sensitive area encompasses the sensitive area previously identified by Feng et al. (2017) and contributes more significantly to improving IOD forecast skill than the individual sea temperature or wind field area.

This study reveals that prioritizing observations in this sensitive area and assimilating these observations into models to improve the accuracy of initial conditions could substantially improve IOD forecast skill. The coupled sensitive area identified in this study provides guidance on where observations should be prioritized. However, given the constraints in observational resources, a critical question remains: how should limited observations be deployed in practice, especially when the coupled sensitive areas vary with the starting months? Previous studies have shown that, in the context of events such as typhoons, targeting observations at locations with the largest initial errors can markedly improve forecast skill (Qin et al., 2022). Meanwhile, Duan et al. (2018) proposed a

quantitative frequency-based method to identify sensitive areas in predictions of two types of El Niño, given the dependence of the sensitive areas on related El Niño types and the starting months. Hindcast experiments confirmed that such an observational array is highly effective in distinguishing two types of El Niño and outperforms the conventional TAO/TRITON array. Building on these insights, one potential strategy involves a three-step process: first, ranking grid points within this sensitive area based on the magnitude of their initial errors in descending order; second, computing the frequency of large-magnitude initial errors among all the starting months; and finally, prioritizing observations at points with both high error values and high frequencies. Whether such a targeted observation strategy can effectively improve IOD forecast skill remains a subject for future research.

6. Summary

This study employs the C-CNOP method to identify sensitive areas of IOD events by incorporating initial coupling uncertainties, and access the effectiveness of the sensitive areas in improving IOD forecast skill.

First, we examine the sensitivity of IOD prediction uncertainties to initial conditions across multiple variables and identify the dominant spatial patterns of initial coupling uncertainties that most cause large prediction uncertainties and significantly limit IOD forecast skill. Initial sea temperature errors are primarily concentrated near the thermocline in the eastern Indian Ocean and western Pacific, while initial zonal wind errors exhibit a distinct east–west dipole pattern over the tropical Indian and Pacific Oceans with maxima localized over the tropical Indian Ocean and tropical western Pacific. These wind errors are strongly coupled with sea temperature errors.

Next, we examine the relationship between prediction errors and initial field similarity in three key areas (IO_Temp, PO_Temp, and UWind). Our results reveal that prediction uncertainties are differentially sensitive to initial errors in these three areas. Furthermore, we constructed ensemble forecasts by selecting members with high initial-field correlation and low errors in the three key areas. Results demonstrate that IOD prediction uncertainties are particularly sensitive to initial errors in the UWind area. Notably, the UWind area shows the highest absolute IMPACT values for the starting months of January (0) and April (0), with values comparable to those of the IO_Temp area for the starting months of October (−1) and July (0). Furthermore, winter and summer prediction errors are most strongly sensitive to initial errors in the UWind area. Forecast skill assessments (ACC) confirm that the UWind area outperforms other areas. This marked improvement underscores the critical role of wind field initialization in IOD prediction, contrasting with prior studies (Feng et al., 2017; Liu et al., 2018; Luo et al., 2007; Wajsowicz, 2005) that emphasized sea temperature initialization.

To further access how initial coupling uncertainties affect IOD predictability, we examine four dynamically coupled areas for each starting month: IO_Temp & IO_UWind, IO_Temp & PO_UWind, PO_Temp & IO_UWind, and PO_Temp & PO_UWind. Among these, the IO_Temp & PO_UWind region yields the highest absolute IMPACT values across all starting months, significantly outperforming the UWind-only area. This finding suggests that the IO_Temp&PO_UWind area yields the highest forecast skill, and this area is the most sensitive area for IOD predictions. Improving the accuracy of initial conditions in this area would most effectively improve IOD forecast skill. The forecast member based on the IO_Temp & PO_UWind area accurately simulates anomalous western Pacific wind fields, perturbing the Walker circulation and inducing anomalous subsidence over the eastern Indian Ocean. This drives surface wind divergence, enhancing upwelling of cold subsurface water. Concurrently, negative subsurface temperature anomalies in the eastern Indian Ocean further amplify cooling, favoring positive IOD development. Comparative analysis with other coupled areas (e.g., PO_Temp & IO_UWind) confirms the superior sensitivity of the IO_Temp & PO_UWind area.

Our findings diverge from previous research by highlighting the critical role of wind field initialization, as well as the importance of initial coupling uncertainties. These insights provide a theoretical foundation for advancing coupled data assimilation and ensemble forecasting in IOD prediction. While our approach eliminates the influence of model errors, bypasses data assimilation, and avoids initial shock effects, future work could employ Observing System Simulation Experiment (OSSE) to future assess the effectiveness of this coupled sensitive area in improving IOD forecast skill. Such experiments, particularly when conducted using alternative coupled models, would help validate the effectiveness of our results. It should be noted that the conclusions of this study are based on the GFDL CM2p1 model only. Although this model has been widely demonstrated to reasonably reproduce key features of the IOD (e.g., Feng et al., 2014), different models exhibit differences in their mean climate states and the strength of coupled feedback. As a result, the precise locations of the identified sensitive

areas may vary across models. The IO_Temp & PO_UWind coupled sensitive area proposed here should therefore be regarded as a physically plausible and strongly supported hypothesis within the context of our modeling framework. Future studies repeating this analysis with different models will be essential to verify the universality of this sensitive area.

Conflict of Interest

The authors declare no conflicts of interest relevant to this study.

Data Availability Statement

The monthly sea temperature and wind field data from the 150-year simulation outputs of the GFDL CM2p1 model, used to identify the sensitive areas associated with IOD events, are available through the Science Data Bank (Feng et al., 2025; downloaded at https://doi.org/10.57760/sciencedb.iap.00014). All analysis scripts used for data processing and figure generation were written using the NCAR Command Language 6.6.2, available at: http://dx.doi.org/10.5065/D6WD3XH5.

Acknowledgments
We thank the three anonymous reviewers for their insightful comments and suggestions. This work was supported by the National Natural Science Foundation of China (Grants 42330111, 42475060, 42450178), and the National Key Scientific and Technological Infrastructure project "Earth System Numerical Simulation Facility" (EarthLab).

References

Bishop, C. H., Etherton, B. J., & Majumdar, S. J. (2001). Adaptive sampling with the ensemble transform Kalman filter. Part I: Theoretical aspects. *Monthly Weather Review*, *129*(3), 420–436. https://doi.org/10.1175/1520-0493(2001)129<0420:aswtet>2.0.co;2

Bishop, C. H., & Toth, Z. (1999). Ensemble transformation and adaptive observations. *Journal of the Atmospheric Sciences*, *56*(11), 1748–1765. https://doi.org/10.1175/1520-0469(1999)056<1748:ETAAO>2.0.CO;2

Burpee, R. W., Franklin, J. L., Lord, S. J., Tuleya, R. E., & Aberson, S. D. (1996). The impact of Omega dropwindsondes on operational hurricane track forecast models. *Bulletin of the American Meteorological Society*, *77*(5), 925–934. https://doi.org/10.1175/1520-0477(1996)077<0925:TIOODO>2.0.CO;2

Cai, W., Yang, K., Wu, L., Huang, G., Santoso, A., Ng, B., et al. (2020). Opposite response of strong and moderate positive Indian Ocean Dipole to global warming. *Nature Climate Change*, *11*(1), 27–32. https://doi.org/10.1038/s41558-020-00943-1

Chen, P., Sun, B., Wang, H., & Zhu, B. (2021). Possible impacts of December Laptev Sea ice on Indian Ocean Dipole conditions during spring. *Journal of Climate*, *34*(16), 6927–6943. https://doi.org/10.1175/JCLI-D-20-0980.1

Delworth, T. L., Broccoli, A. J., Rosati, A., Stouffer, R. J., Balaji, V., Beesley, J. A., et al. (2006). GFDL's CM2 global coupled climate models. Part I: Formulation and simulation characteristics. *Journal of Climate*, *19*(5), 643–674. https://doi.org/10.1175/jcli3629.1

Du, Y., Zhang, Y., Zhang, L., Tozuka, T., Ng, B., & Cai, W. (2020). Thermocline warming induced extreme Indian Ocean Dipole in 2019. *Geophysical Research Letters*, *47*(18), e2020GL090079. https://doi.org/10.1029/2020GL090079

Duan, W. S., Hu, L., & Feng, R. (2024). Coupled conditional nonlinear optimal perturbations and their application to ENSO ensemble forecasts. *Science China Earth Sciences*, *67*(3), 826–842. https://doi.org/10.1007/s11430-023-1273-1

Duan, W. S., Li, X., & Tian, B. (2018). Towards optimal observational array for dealing with challenges of El Niño-Southern Oscillation predictions due to diversities of El Niño. *Climate Dynamics*, *51*(9–10), 3351–3368. https://doi.org/10.1007/s00382-018-4082-x

Feng, R., Duan, W., & Hu, J. (2025). A dataset of 150-year GFDL CM2p1 simulation [Dataset]. *Science Data Bank*. https://doi.org/10.57760/sciencedb.iap.00014

Feng, R., & Duan, W. S. (2019). Indian Ocean Dipole-related predictability barriers induced by initial errors in the tropical Indian Ocean in a CGCM. *Advances in Atmospheric Sciences*, *36*(6), 658–668. https://doi.org/10.1007/s00376-019-8224-9

Feng, R., Duan, W. S., & Mu, M. (2017). Estimating observing locations for advancing beyond the winter predictability barrier of Indian Ocean dipole event predictions. *Climate Dynamics*, *48*(3–4), 1173–1185. https://doi.org/10.1007/s00382-016-3134-3

Feng, R., Mu, M., & Duan, W. S. (2014). Study on the "winter persistence barrier" of Indian Ocean dipole events using observation data and CMIP5 model outputs. *Theoretical and Applied Climatology*, *118*(3), 523–534. https://doi.org/10.1007/s00704-013-1083-x

GFDL Global Atmospheric Model Development Team. (2004). The new GFDL global atmosphere and land model AM2–LM2: Evaluation with prescribed SST simulations. *Journal of Climate*, *17*, 4641–4673.

Griffies, S. M. (2009). *Elements of MOM4p1: GFDL ocean group. Technical Report No. 6*. NOAA/Geophysical Fluid Dynamics Laboratory.

Hamill, T. M., & Snyder, C. (2002). Using improved background-error covariance from an ensemble Kalman filter for adaptive observations. *Monthly Weather Review*, *130*(6), 1552–1572. https://doi.org/10.1175/1520-0493(2002)130<1552:UIBECF>2.0.CO;2

Huang, B., Su, T., Qu, S., Zhang, H., Hu, S., & Feng, G. (2021). Strengthened relationship between tropical Indian Ocean dipole and subtropical Indian Ocean dipole after the late 2000s. *Geophysical Research Letters*, *48*(19), e2021GL094835. https://doi.org/10.1029/2021GL094835

Hui, C., & Zheng, X. T. (2018). Uncertainty in Indian Ocean Dipole response to global warming: The role of internal variability. *Climate Dynamics*, *51*(9–10), 3597–3611. https://doi.org/10.1007/s00382-018-4098-2

Jiang, F., Zhang, W., Jin, F. F., Stuecker, M. F., & Allan, R. (2021). El Niño pacing orchestrates inter-basin Pacific-Indian Ocean interannual connections. *Geophysical Research Letters*, *48*(19), e2021GL095242. https://doi.org/10.1029/2021GL095242

Kim, H. M., Morgan, M. C., & Morss, R. E. (2004). Evolution of analysis error and adjoint-based sensitivities: Implications for adaptive observations. *Journal of the Atmospheric Sciences*, *61*(7), 795–812. https://doi.org/10.1175/1520-0469(2004)061<0795:eoaeaa>2.0.co;2

Leutbecher, M., & Palmer, T. N. (2008). Ensemble forecasting. *Journal of Computational Physics*, *227*(7), 3515–3539. https://doi.org/10.1016/j.jcp.2007.02.014

Li, Y., Qiu, Y., Hu, J., Aung, C., Lin, X., Jing, C., & Zhang, J. (2021). The strong upwelling event off the southern coast of Sri Lanka in 2013 and its relationship with Indian Ocean Dipole events. *Journal of Climate*, *34*(9), 3555–3569. https://doi.org/10.1175/JCLI-D-20-0620.s1

Liu, D., Duan, W., Feng, R., & Tang, Y. (2018). "Summer predictability barrier" of Indian Ocean dipole events and corresponding error growth dynamics. *Journal of Geophysical Research: Ocean*, *123*(5), 3635–3650. https://doi.org/10.1029/2017JC013739

Liu, D., Duan, W. S., & Feng, R. (2021). How does El Nino affect predictability barrier of its accompanied positive Indian Ocean Dipole event? *Journal of Marine Science and Engineering*, *9*(11), 1169. https://doi.org/10.3390/jmse9111169

Lu, B., Ren, H., Scaife, A. A., Wu, J., Dunstone, N., Smith, D., et al. (2018). An extreme negative Indian Ocean Dipole event in 2016: Dynamics and predictability. *Climate Dynamics*, *51*(1–2), 89–100. https://doi.org/10.1007/s00382-017-3908-2

Luo, J. J., Masson, S., Behera, S., & Yamagata, T. (2007). Experimental forecasts of the Indian Ocean dipole using a coupled OAGCM. *Journal of Climate*, *20*(10), 2178–2190. https://doi.org/10.1175/JCLI4132.1

Milly, P. C. D., & Shmakin, A. B. (2002). Global modeling of land water and energy balances. Part I: The land dynamics (LaD) model. *Journal of Hydrometeorology*, *3*(3), 283–299. https://doi.org/10.1175/1525-7541(2002)003<0283:gmolwa>2.0.co;2

Mu, M., & Duan, W. S. (2003). A new approach to studying ENSO predictability: Conditional nonlinear optimal perturbation. *Chinese Science Bulletin*, *48*(10), 1045–1047. https://doi.org/10.1360/02wd0389

Mu, M., Duan, W. S., & Wang, B. (2003). Conditional nonlinear optimal perturbation and its applications. *Nonlinear Processes in Geophysics*, *10*, 493–501. https://doi.org/10.5194/npg-10-493-2003

Mu, M., Zhou, F., & Wang, H. A. (2009). Method for identifying the sensitive areas in targeted observations for tropical cyclone prediction: Conditional nonlinear optimal perturbation. *Monthly Weather Review*, *137*(5), 1623–1639. https://doi.org/10.1175/2008mwr2640.1

Qin, X., Duan, W., Chan, P. W., Chen, B., & Huang, K. N. (2022). Effects of dropsonde data in field campaigns on forecasts of tropical cyclones over the western North Pacific in 2020 and role of CNOP sensitivity. *Advances in Atmospheric Sciences*, *40*(5), 791–803. https://doi.org/10.1007/s00376-022-2136-9

Qin, X., & Mu, M. (2012). Influence of conditional nonlinear optimal perturbations sensitivity on typhoon track forecasts. *Quarterly Journal of the Royal Meteorological Society*, *138*(662), 185–197. https://doi.org/10.1002/qj.902

Qiu, Y., Cai, W. J., Guo, X. G., & Ng, B. (2014). The asymmetric influence of the positive and negative IOD events on China's rainfall. *Scientific Reports*, *4*(1), 4943. https://doi.org/10.1038/srep04943

Saji, N. H., Goswami, B. N., Vinayachandran, P. N., & Yamagata, T. (1999). A dipole mode in the tropical Indian Ocean. *Nature*, *401*(6751), 360–363. https://doi.org/10.1038/43854

Sang, Y. F., Singh, V. P., & Xu, K. (2019). Evolution of IOD-ENSO relationship at multiple time scales. *Theoretical and Applied Climatology*, *136*(3–4), 1303–1309. https://doi.org/10.1007/s00704-018-2557-7

Shi, L., Hendon, H. H., Alves, O., Luo, J. J., Balmaseda, M., & Anderson, D. (2012). How predictable is the Indian Ocean dipole? *Monthly Weather Review*, *140*(12), 3867–3884. https://doi.org/10.1175/MWR-D-12-00001.1

Stouffer, R. J., Broccoli, A. J., Delworth, T. L., Dixon, K. W., Gudgel, R., Held, I., et al. (2006). GFDL's CM2 global coupled climate models. Part IV: Idealized climate response. *Journal of Climate*, *19*(5), 723–740. https://doi.org/10.1175/JCLI3632.1

Wajsowicz, R. C. (2004). Climate variability over the tropical Indian Ocean sector in the NSIPP seasonal forecast system. *Journal of Climate*, *17*(24), 4783–4804. https://doi.org/10.1175/jcli-3239.1

Wajsowicz, R. C. (2005). Potential predictability of tropical Indian Ocean SST anomalies. *Geophysical Research Letters*, *32*(24), L24702. https://doi.org/10.1029/2005GL024169

Wang, Q., Mu, M., & Dijkstra, H. A. (2013). The similarity between optimal precursor and optimally growing initial error in prediction of Kuroshio large meander and its application to targeted observation. *Journal of Geophysical Research: Ocean*, *118*(2), 869–884. https://doi.org/10.1002/jgrc.20084

Webster, P. J., Moore, A. M., Loschnigg, J. P., & Leben, R. R. (1999). Coupled ocean-atmosphere dynamics in the Indian Ocean during 1997–1998. *Nature*, *401*(6751), 356–360. https://doi.org/10.1038/43848

Wittenberg, A. T., Rosati, A., Lau, N. C., & Ploshay, J. J. (2006). GFDL's CM2 global coupled climate models. Part III: Tropical pacific climate and ENSO. *Journal of Climate*, *19*(5), 698–722. https://doi.org/10.1175/JCLI3631.1

Wu, C. C., Lin, P. H., Aberson, S., Yeh, T. C., Huang, W. P., Chou, K. H., et al. (2005). Dropwindsonde observations for typhoon surveillance near the Taiwan region (DOTSTAR): An overview. *Bulletin of the American Meteorological Society*, *86*, 787–790. https://doi.org/10.1175/BAMS-86-6-787

Xiao, F., Wang, D., & Leung, M. Y. (2020). Early and extreme warming in the South China Sea during 2015/2016: Role of an unusual Indian Ocean Dipole event. *Geophysical Research Letters*, *47*(17), e2020GL089936. https://doi.org/10.1029/2020GL089936

Yang, J. L., Liu, Q. Y., & Liu, Z. Y. (2010). Linking observations of the Asian Monsoon to the Indian Ocean SST: Possible roles of Indian Ocean basin mode and dipole mode. *Journal of Climate*, *23*(21), 5889–5902. https://doi.org/10.1175/2010jcli2962.1

Yang, Y., Xie, S. P., Wu, L., Kosaka, Y., Lau, N. C., & Vecchi, G. A. (2015). Seasonality and predictability of the Indian Ocean Dipole mode: ENSO forcing and internal variability. *Journal of Climate*, *28*(20), 8021–8036. https://doi.org/10.1175/jcli-d-15-0078.1

Yu, Y., Mu, M., Duan, W., & Gong, T. (2012). Contribution of the location and spatial pattern of initial error to uncertainties in El Nino predictions. *Journal of Geophysical Research*, *117*(C6), C06018. https://doi.org/10.1029/2011JC007758

Yuan, D., Xu, P., & Xu, T. (2017). Climate variability and predictability associated with the Indo-Pacific oceanic channel dynamics in the CCSM4 coupled system model. *Chinese Journal of Oceanology and Limnology*, *35*(1), 23–38. https://doi.org/10.1007/s00343-016-5178-y

Zhang, W., Wang, Y., Jin, F. F., Stuecker, M. F., & Turner, A. G. (2015). Impact of different El Niño types on the El Niño/IOD relationship. *Geophysical Research Letters*, *42*(20), 8570–8576. https://doi.org/10.1002/2015gl065703

Zhao, S., Stuecker, M. F., Jin, F. F., Feng, J., Ren, H., Zhang, W., & Li, J. (2020). Improved predictability of the Indian Ocean Dipole using a stochastic dynamical model compared to the North American multimodel ensemble forecast. *Weather and Forecasting*, *35*(2), 379–399. https://doi.org/10.1175/WAF-D-19-0184.1

Zhu, J., Huang, B., Kumar, A., & Kinter, J. L. (2015). Seasonality in prediction skill and predictable pattern of tropical Indian Ocean SST. *Journal of Climate*, *28*(20), 7962–7984. https://doi.org/10.1175/jcli-d-15-0067.1